

# L4DR: LiDAR-4DRadar Fusion for Weather-Robust 3D Object Detection

Xun Huang<sup>1</sup>, Ziyu Xu<sup>1</sup>, Hai Wu<sup>1</sup>, Jinlong Wang<sup>1</sup>, Qiming Xia<sup>1</sup>,  
Yan Xia<sup>2</sup>, Jonathan Li<sup>3</sup>, Kyle Gao<sup>3</sup>, Chenglu Wen<sup>1\*</sup>, Cheng Wang<sup>1</sup>

<sup>1</sup> Xiamen University,

<sup>2</sup> Technische Universität München

<sup>3</sup> University of Waterloo

## Abstract

LiDAR-based vision systems are integral for 3D object detection, which is crucial for autonomous navigation. However, they suffer from performance degradation in adverse weather conditions due to the quality deterioration of LiDAR point clouds. Fusing LiDAR with the weather-robust 4D radar sensor is expected to solve this problem. However, the fusion of LiDAR and 4D radar is challenging because they differ significantly in terms of data quality and the degree of degradation in adverse weather. To address these issues, we introduce L4DR, a weather-robust 3D object detection method that effectively achieves LiDAR and 4D Radar fusion. Our L4DR includes **Multi-Modal Encoding (MME)** and **Foreground-Aware Denoising (FAD)** technique to reconcile sensor gaps, which is the first exploration of the complementarity of early fusion between LiDAR and 4D radar. Additionally, we design an **Inter-Modal** and **Intra-Modal** ( $\{IM\}^2$ ) parallel feature extraction backbone coupled with a **Multi-Scale Gated Fusion (MSGF)** module to counteract the varying degrees of sensor degradation under adverse weather conditions. Experimental evaluation on a VoD dataset with simulated fog proves that L4DR is more adaptable to changing weather conditions. It delivers a significant performance increase under different fog levels, improving the 3D mAP by up to 19.99% over the traditional LiDAR-only approach. Moreover, the results on the K-Radar dataset validate the consistent performance improvement of L4DR in real-world adverse weather conditions.

## Introduction

3D object detection is fundamental to vision systems of unmanned platforms, extensively utilized in applications such as intelligent robots navigation (Ghita et al. 2024; Xu et al. 2022) and autonomous driving (Bijelic et al. 2020). Full Driving Automation (FDA, Level 5) relies on weather-robust 3D object detection, providing precise 3D bounding boxes even under various challenging adverse weather conditions (Qian et al. 2021). Owing to the high resolution and strong interference resistance of LiDAR sensors, LiDAR-based 3D object detection has emerged as a mainstream area of research (Yan et al. 2023; Xia et al. 2023; Wu et al. 2024). However, LiDAR sensors exhibit considerable sensitivity to weather conditions. In adverse scenarios such as rain and

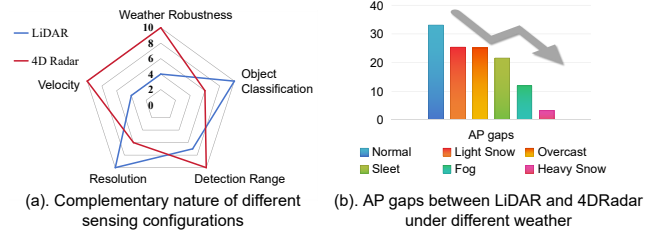


Figure 1: (a) The radar chart illustrates the complementary nature of LiDAR and 4D radar sensors. (b) AP gaps between LiDAR and 4D radar in real different weather (the extent to which LiDAR is superior to 4D radar).

fog, the scanning signals suffer from substantial degradation and increased noise (Huang et al. 2024; Hahner et al. 2021). This degradation can negatively impact 3D detectors, compromising the reliability of autonomous perception systems.

Aside from LiDAR, 4D (range, azimuth, Doppler, and elevation) millimeter-wave radar has increasingly been recognized (Han et al. 2023; Sun and Zhang 2021). As shown in Figure 1 (a), 4D radar outperforms LiDAR in weather robustness, velocity measurement, and detection range. The millimeter-wave signals of 4D radar have wavelengths much larger than the tiny particles that form fog, rain, and snow (Golovachev et al. 2018; Balal, Pinhasi, and Pinhasi 2016), exhibiting reduced susceptibility to weather disturbances. As shown in Fig. 1 (b), the performance gap between LiDAR and 4D radar decreases as the severity of the weather rises. Therefore, the 4D radar sensor is suitable for various weather conditions. However, LiDAR is still far ahead of the radar in the important metrics of object classification and resolution. These circumstances make it very feasible to promote the full fusion of 4D radar and LiDAR data to improve 3D object detection. Pioneering approaches such as InterFusion (Wang et al. 2022b), M<sup>2</sup>Fusion (Wang et al. 2022a), and 3D-LRF (Chae, Kim, and Yoon 2024) represent the initial explorations into the fusion of LiDAR and 4D radar, showing significant performance improvements compared to models employing LiDAR-only or 4D radar-only.

\*Corresponding author.

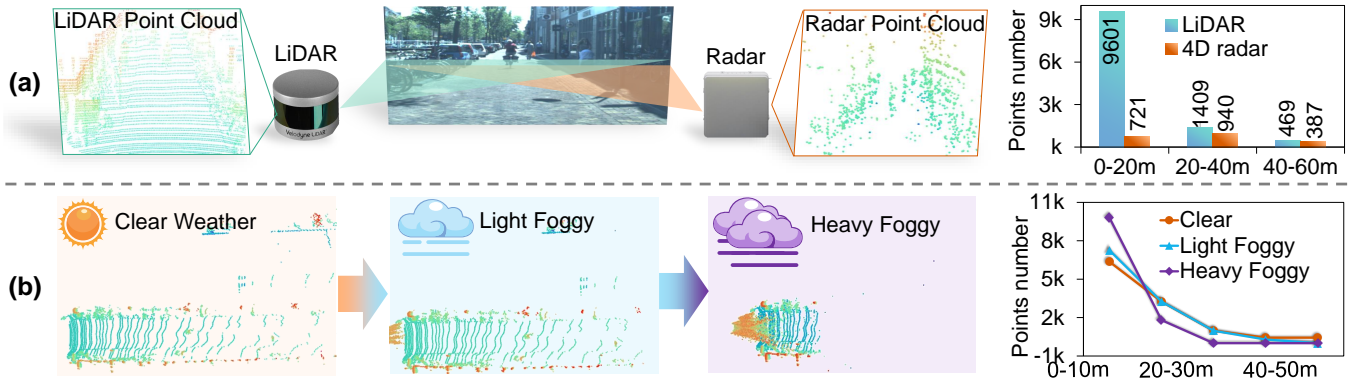


Figure 2: The challenges of fusing LiDAR and 4D radar in adverse weather conditions. (a) Significant quality disparity between the LiDAR and the 4D radar. (b) Severe degradation of LiDAR data quality in adverse weather.

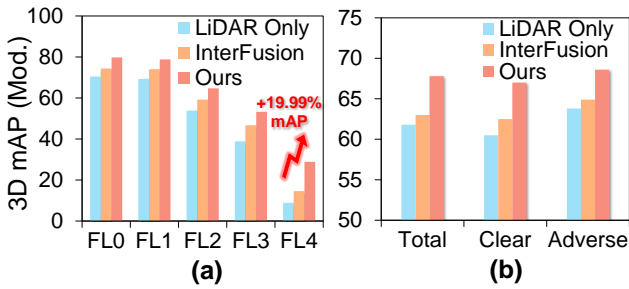


Figure 3: Performance comparison of our L4DR and LiDAR-only in (a) various simulated fog levels (FL denotes fog level) and (b) real-world adverse weather.

Despite these advances, the fusion of LiDAR and 4D radar sensors has not addressed the substantial disparities in data quality and the different degrees of degradation in adverse weather. As shown in Figure 2 (a), a primary challenge arises from the significant quality disparity between the LiDAR sensor and the 4D radar sensor. A second challenge pertains to varying sensor degradation under adverse weather conditions. Figure 2 (b) shows LiDAR sensors undergo severe data degradation in adverse weather. Conversely, the data quality decrease in 4D radar is significantly lower (Han et al. 2023; Sun and Zhang 2021) (Details of real-world LiDAR and 4D radar point cloud distributions under different weather conditions are given in Supplementary Material A.1.). This motivates the consideration of emphasizing LiDAR and 4D radar sensors with varying degrees while considering weather conditions during data fusion. The substantial data quality disparities and different degrees of sensor degradation is not properly addressed in existing LiDAR and 4D radar fusion methods in adverse weather conditions.

To address the challenges above, we propose L4DR, a weather-robust 3D object detection via LiDAR and 4D radar fusion. We designed a Multi-Modal Encoder (MME) module and a Foreground-Aware Denoising (FAD) to address the substantial data quality disparities. This innovation pioneers the use of early data-level fusion strategies to mitigate the

disparities between LiDAR and 4D radar while concurrently improving the data quality from each modality. In response to the varying degrees of sensor degradation under diverse weather conditions, L4DR incorporates the Inter-Modal and Intra-Modal ( $\{IM\}^2$ ) backbone and the Multi-Scale Gated Fusion (MSGF) module, adaptively focusing on the significant modal features in different weather conditions.

In Figure 3, our comprehensive testing on VoD (Palffy et al. 2022) and K-Radar datasets (Paek, Kong, and Wijaya 2022) showcase the resilience and superior performance of L4DR across various simulated and real-world adverse weather disturbances. Our main contributions are as follows:

- We introduce the innovative Multi-Modal Encoder (MME) module, which achieves LiDAR and 4D radar fusion without resorting to error-prone processes (e.g., depth estimation, height compression). This approach effectively bridges the substantial LiDAR and 4D radar data quality disparities.
- We designed an  $\{IM\}^2$  backbone with a Multi-Scale Gated Fusion (MSGF) module, adaptively extracting salient features from LiDAR and 4D radar sensors under various weather conditions. This enables the model to adapt to varying levels of sensor degradation under adverse weather conditions.
- Extensive experiments on the two benchmarks, VoD and K-Radar, demonstrate the effectiveness of our L4DR under various levels and types of adverse weather, achieving new state-of-the-art performances on both datasets.

## Related work

**LiDAR-based 3D object detection.** Researchers have developed single-stage and two-stage methods to tackle challenges for 3D object detection. Single-stage detectors such as VoxelNet (Yan, Mao, and Li 2018), PointPillars (Lang et al. 2019), 3DSSD (Yang et al. 2020), DSVT (Wang et al. 2023a) utilize PointNet++ (Qi et al. 2017), sparse convolution, or other point feature encoder to extract features from point clouds and perform detection in the Bird’s Eye View (BEV) space. Conversely, methods such as PV-RCNN (Shi et al. 2020), PV-RCNN++ (Shi et al. 2022), Voxel-RCNN

(Deng et al. 2021), and VirConv (Wu et al. 2023) focus on two-stage object detection, integrating RCNN networks into 3D detectors. Even though these mainstream methods have gained excellent performance in normal weather, they lack robustness and still need improvement under various adverse weather conditions.

**LiDAR-based 3D object detection in adverse weather.** LiDAR sensors may undergo degradation under adverse weather conditions such as snow, fog, and rain. Physics-based simulations (Teufel et al. 2022; Hahner et al. 2022, 2021; Kilic et al. 2021) have been explored to reproduce point clouds under adverse weather to alleviate the issue of data scarcity. (Charron, Phillips, and Waslander 2018; Heinzer et al. 2020) utilized the DROR, DSOR, or convolutional neural networks (CNNs) to classify and filter LiDAR noise points. (Xu et al. 2021) designed a general completion framework that addresses the problem of domain adaptation across different weather conditions. (Huang et al. 2024) designed a general knowledge distillation framework that transfers sunny performance to rainy performance. However, these methods primarily rely on single-LiDAR modal data, which will be constrained by the decline in the quality of LiDAR under adverse weather conditions.

**LiDAR-radar fusion-based 3D object detection.** LiDAR-radar fusion for 3D object detection has gained increasing attention in recent years. MVDNet (Qian et al. 2021) has designed a framework for fusing LiDAR and radar. ST-MVDNet (Li et al. 2022) and ST-MVDNet++ (Li, O’Toole, and Kitani 2023) incorporate a self-training teacher-student to MVDNet to enhance the model. Bi-LRFusion (Wang et al. 2023b) framework employs a bidirectional fusion strategy to improve dynamic object detection performance. However, these studies only focus on 3D radar and LiDAR. As research progresses, the newest studies continue to drive the development of LiDAR-4D radar fusion. M<sup>2</sup>-Fusion (Wang et al. 2022a) and InterFusion (Wang et al. 2022b) explore new LiDAR and 4D radar fusion approaches. However, these methods have not considered and overcome the challenges of fusing 4D radar and LiDAR under adverse weather conditions to promote weather-robust 3D object detection.

## Methodology

### Problem statement and overall design

**LiDAR-4D radar fusion-based 3D object detection.** For an outdoor scene, we denote a LiDAR point cloud as  $\mathcal{P}^l = \{p_i^l\}_{i=1}^{N_l}$ ,  $p_i^l = \{x_i, y_i, z_i, \{C_i^l\}\}$  and a 4D radar point cloud as  $\mathcal{P}^r = \{p_i^r\}_{i=1}^{N_r}$ ,  $p_i^r = \{x_i, y_i, z_i, \{C_i^r\}\}$ , where  $i$  indexes individual points,  $x, y, z$  denote 3D world coordinates, and  $N^m$  and  $C^m$  denote the number of points and the point-wise initial data features of modality  $m \in \{l, r\}$  ( $l$  for LiDAR and  $r$  for radar). Subsequently, a multi-modal model  $\mathcal{M}$  extract deep features  $\mathcal{F}^m$  from  $\mathcal{P}^m$ , written as  $\mathcal{F}^m = g(f_{\mathcal{M}}(\mathcal{P}^m; \Theta))$ . The objective of 3D object detection is to regress the 3D bounding boxes  $B = \{b_i\}_{i=1}^{N_b}$ ,  $B \in \mathbb{R}^{N_b \times 7}$ , using fused feature  $\mathcal{F}^f = \phi(\mathcal{F}^l, \mathcal{F}^r)$ , where  $\phi$  donates fusion method. Each box  $b_i$  is encoded using 3D coordinates, size, and orientation, denoted by  $b_i = \{x_i, y_i, z_i, l_i, w_i, h_i, \theta_i\}$ .

**Significant quality disparities between LiDAR and 4D radar sensors** . As mentioned before, there is a huge difference between  $\mathcal{P}^l$  and  $\mathcal{P}^r$  in the same scene. Specifically, we use the Chamfer Distance ( $d_{CD}$ ) (Borgefors 1986) to quantitatively measure the point cloud distance between  $\mathcal{P}^l$  and  $\mathcal{P}^r$  in the VoD (Palffy et al. 2022) dataset. The result of  $d_{CD}(\mathcal{P}^l, \mathcal{P}^r)$  is 342.6 m between the LiDAR and 4D Radar point clouds even in the same scene, indicating a significant difference between  $\mathcal{P}^l$  and  $\mathcal{P}^r$ . This data quality disparities phenomenon poses a significant challenge to data fusion.

To fully fuse two modalities, one possible solution is to use  $\mathcal{P}^l$  to enhance the highly sparse  $\mathcal{P}^r$  that lacks discriminative details. Therefore, our L4DR includes a **Multi-Modal Encoder (MME)**, Figure 4(a)), which performs early-fusion complementarity at the data encoder level. However, we found that direct data fusion would also cause much of the noise in  $\mathcal{P}^r$  to spread to  $\mathcal{P}^l$ . Therefore, we integrated **Foreground-Aware Denoising (FAD)**, Figure 4(b)) into L4DR before MME to filter out most of the noise in  $\mathcal{P}^r$ .

**Significant degradation of LiDAR sensor in adverse weather conditions** . Compared to 4D radar, the quality of LiDAR point cloud  $\mathcal{P}^l$  is more easily affected by adverse weather conditions, leading to lower data quality and varying feature presentations  $\mathcal{F}^l$ . Taking foggy weather as an example, we conducted four levels of fog simulations (Hahner et al. 2021) (denoted as  $\psi$ ) on the VoD dataset to simulate different degrees of foggy weather. The simulated LiDAR data is denoted as  $\mathcal{P}_{\mathcal{L}}^l = \psi(\mathcal{P}^l, \mathcal{L})$ ,  $\mathcal{L} \in [0, 4]$  indicating the level of fog simulation with zero representing clear weather. Subsequently, cosine similarity  $S_{cos}$  was used to quantitatively measure the similarity between features  $\mathcal{F}_{\mathcal{L}}^l$  under different levels of fog simulation  $\mathcal{L}$ , to the features at fog level zero  $\mathcal{F}_0^l$  in the same scene. The cosine similarity is given as

$$S_{cos}(\mathcal{F}_0^l, \mathcal{F}_{\mathcal{L}}^l) = \frac{\mathcal{F}_0^l \cdot \mathcal{F}_{\mathcal{L}}^l}{\|\mathcal{F}_0^l\| \times \|\mathcal{F}_{\mathcal{L}}^l\|}, \quad (1)$$

The results in Table 1 show that the degree of variation in  $\mathcal{F}^l$  is significantly affected by fog level  $\mathcal{L}$  in different convolutional layers  $\mathcal{D}$ . In real-world scenarios where weather conditions are subject to constant change, the feature presentation  $\mathcal{F}^l$  is frequently varying, which will also affect the presentation of the fusion feature  $\mathcal{F}^f$ . This phenomenon has a detrimental impact on the weather-robust stability advantage of  $\mathcal{F}^r$ , which in turn impedes the realization of a weather-robust 3D detector.

Layer Index	$\overline{S_{cos}}(\mathcal{F}_0^l, \mathcal{F}_1^l)$	$\overline{S_{cos}}(\mathcal{F}_0^l, \mathcal{F}_2^l)$	$\overline{S_{cos}}(\mathcal{F}_0^l, \mathcal{F}_3^l)$	$\overline{S_{cos}}(\mathcal{F}_0^l, \mathcal{F}_4^l)$
$\mathcal{D} = 0$ (BEV)	0.84(↓0.16)	0.64(↓0.36)	0.52(↓0.48)	0.27(↓0.73)
$\mathcal{D} = 1$	0.95(↓0.05)	0.83(↓0.17)	0.72(↓0.28)	0.57(↓0.43)
$\mathcal{D} = 2$	0.98(↓0.02)	0.87(↓0.13)	0.77(↓0.23)	0.73(↓0.27)
$\mathcal{D} = 3$	0.99(↓0.01)	0.93(↓0.07)	0.71(↓0.29)	0.65(↓0.35)

Table 1: The cosine similarity of VoD dataset LiDAR features under different concentrations of adverse weather with respect to features under clear weather.

Previous backbones focusing solely on fused inter-modal features  $\mathcal{F}^f$  overlook the strengths of each modality, leading to challenges in addressing the frequent fluctuation of

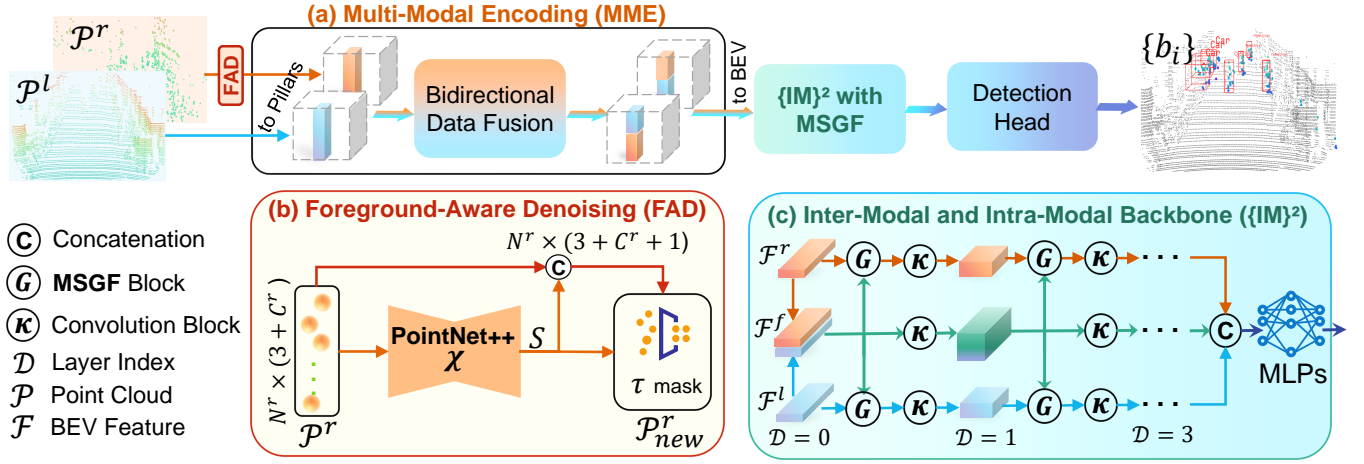


Figure 4: L4DR framework. (a) **Multi-Modal Encoder (MME)** fuses bi-directional data for both LiDAR and 4D radar modalities at the Encoder stage to obtain higher quality BEV features. Next, (b) **Foreground-Aware Denoising (FAD)** performs denoising by segmenting foreground semantics per 4D radar point. Finally, (c) **Inter-Modal and Intra-Modal ({IM})<sup>2</sup>** backbone coupled with **Multi-Scale Gated Fusion (MSGF)** uses a gating strategy to filter features to avoid redundant information while extracting inter-modal and intra-modal features in parallel.

$\mathcal{F}^l$ . To address this issue and ensure robust fusion across diverse weather conditions, we introduce the **Inter-Modal and Intra-Modal ({IM})<sup>2</sup>**, Figure 4 (c)) backbone. This design simultaneously emphasizes inter-modal and intra-modal features, enhancing model adaptability. However, redundancy between these features arises. Drawing inspiration from gated fusion techniques (Hosseinpour, Samadzadegan, and Javan 2022; Song, Zhao, and Skinner 2024a), we propose the **Multi-Scale Gated Fusion (MSGF)**, Figure 4 (d)) module. MSGF utilizes inter-modal features  $\mathcal{F}^f$  to filter intra-modal features  $\mathcal{F}^l$  and  $\mathcal{F}^r$ , effectively reducing feature redundancy. Our experimental results in Table. 5 shows the {IM}<sup>2</sup> and MSGF modules significantly enhance the model’s capability to adapt to varying adverse weather conditions, ensuring the ability of weather-robustness.

### Foreground-Aware Denoising (FAD)

Due to multipath effects, 4D radar contains significant noise points. Despite applying the Constant False Alarm Rate (CFAR) algorithm to filter out noise during the data acquisition process, the noise level remains substantial. It is imperative to further reduce the clutter noise in 4D radar data before early data fusion to avoid noise spreading. Considering the minimal contribution of background points to object detection, this work introduces point-level foreground semantic segmentation to 4D radar denoising, performing a Foreground-Aware Denoising. Specifically, we first utilize PointNet++ (Qi et al. 2017) combined with a segmentation head as  $\chi$ , to predict the foreground semantic probability  $S = \chi(\mathcal{P}^r)$  for each point in the 4D radar. Subsequently, points with a foreground probability below a predefined threshold  $\tau$  are filtered out, that is  $\mathcal{P}_{new}^r = \{p_i^r | S_i \geq \tau\}$ . FAD effectively filters out as many noise points as possible while preventing the loss of foreground points.

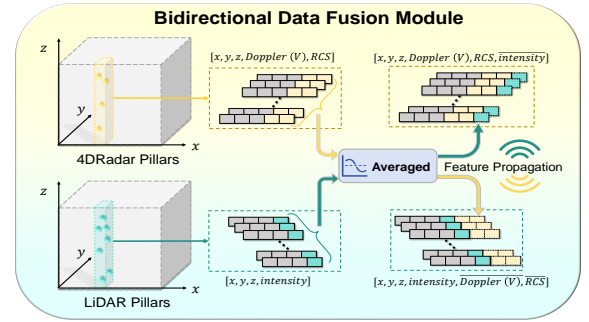


Figure 5: Bidirectional Data Fusion in MME. LiDAR-specific point features (blue) and radar-specific point features (red) located in the same pillar are averaged (Avg.) for feature propagation. And the cross-modal offsets (CMO) are computed to enrich the geometric features.

### Multi-Modal Encoder (MME)

Even following denoising using FAD, there remains a significant quality disparity between LiDAR and 4D radar due to limitations in resolution. We thus design a Multi-Modal Encoder module that fuses LiDAR and radar points at an early stage to extract richer features.

As illustrated in Figure 5, we first refer (Lang et al. 2019) to encode the LiDAR point cloud into a pillar set  $\mathcal{P}^l = \{p_i^l\}_{i=1}^N$ . Each LiDAR point  $p_{(i,j)}^l$  in pillar  $p_i^l$  encoded using encoding feature  $f_{(i,j)}^l$  as

$$f_{(i,j)}^l = [\mathbf{x}^l, \mathbf{y}_{cl}^l, \mathbf{z}^l, \lambda], \quad (2)$$

where  $\mathbf{x}^l = [x^l, y^l, z^l]$  is the coordinate of the LiDAR point,  $\mathbf{y}_{cl}^l$  denotes the distance from the LiDAR point to the arithmetic mean of all LiDAR points in the pillar,  $\mathbf{z}^l$  denotes the



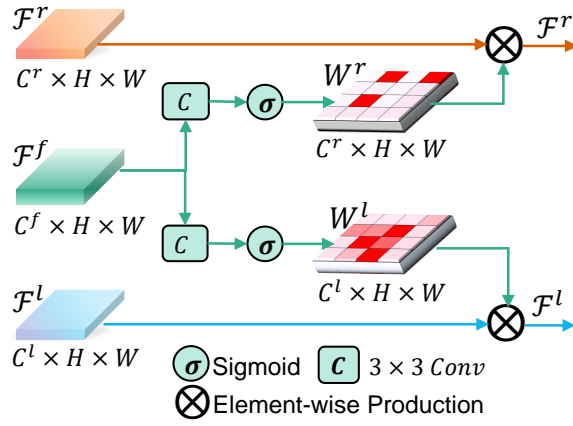


Figure 6: Gated fusion block in our MSGF. The gated block processes input features from LiDAR and 4D radar by using the fused inter-modal features. It generates adaptive gating weights from fused features and applies these weights via element-wise multiplication to filter out redundant information in intra-modal features.

(horizontal) offset from the pillar center in  $x, y$  coordinates, and  $\lambda$  is the reflectance. Similarly, each 4D radar point  $p_{(i,j)}^r$  in pillar  $p_i^r$  encoded using encoding feature  $f_{(i,j)}^r$  as

$$f_{(i,j)}^r = [\mathcal{X}^r, \mathcal{Y}_{cr}^r, \mathcal{Z}^r, \mathcal{V}, \Omega], \quad (3)$$

where  $\mathcal{X}^r$ ,  $\mathcal{Y}_{cr}^r$ , and  $\mathcal{Z}^r$  are similar in meaning to those in Eq.2.  $\mathcal{V} = [\mathcal{V}_x, \mathcal{V}_y]$  is Doppler information along each axis, and  $\Omega$  is Radar Cross-Section (RCS).

We then perform cross-modal feature propagation for LiDAR pillar encoding features  $f_{(i,j)}^l$  and radar pillar encoding features  $f_{(i,j)}^r$  that occupy the same coordinates. The fused LiDAR pillar encoding features  $\hat{f}_{(i,j)}^l$  and 4D radar points  $\hat{f}_{(i,j)}^r$  are obtained by fusing  $f_{(i,j)}^l$  and  $f_{(i,j)}^r$  as follows:

$$\begin{aligned} \hat{f}_{(i,j)}^l &= [\mathcal{X}^l, \mathcal{Y}_{cl}^l, \mathcal{Y}_{cr}^l, \mathcal{Z}^l, \lambda, \bar{\mathcal{V}}, \bar{\Omega}], \\ \text{and } \hat{f}_{(i,j)}^r &= [\mathcal{X}^r, \mathcal{Y}_{cl}^r, \mathcal{Y}_{cr}^r, \mathcal{Z}^r, \bar{\lambda}, \bar{\mathcal{V}}, \Omega], \end{aligned} \quad (4)$$

where the overline denotes the average of all point features of another modality in that pillar.

The feature propagation is beneficial because  $\lambda$  and  $\Omega$  are helpful for object classification, while Doppler information  $\mathcal{V}$  is crucial for distinguishing dynamic objects (Song, Zhao, and Skinner 2024b). Cross-modal feature sharing makes comprehensive use of these advantages and cross-modal offsets  $[\mathcal{Y}_{cl}^m, \mathcal{Y}_{cr}^m]$ ,  $m \in \{l, r\}$  also further enrich the geometric information. This MME method compensates for the data quality of 4D radar under normal weather conditions and can also enhance the quality of LiDAR in adverse weather, providing richer information for feature extraction. Subsequently, we applied a linear layer and max pooling operations to the fused pillar encoding features  $\hat{f}$  to obtain the corresponding modal BEV features  $\mathcal{F}$ .

## {IM}<sup>2</sup> Backbone and MSGF Block

To take full advantage of the respective advantages of LiDAR and 4D radar, it is necessary to focus on both inter-modal features and intra-modal features. We introduce the **Inter-Modal** and **Intra-Modal** backbone ({IM}<sup>2</sup>). {IM}<sup>2</sup> serves as a multi-modal branch feature extraction module that concurrently extracts inter-modal feature ( $\mathcal{F}^f$ ) and intra-modal features ( $\mathcal{F}^l, \mathcal{F}^r$ ). Specifically, we fuse two Intra-Modal features to form an Inter-Modal feature,

$$\mathcal{F}^f = \phi(\mathcal{F}^l, \mathcal{F}^r), \quad (5)$$

where  $\phi$  denotes fusion approach (we use concatenation). Subsequently, we apply a convolutional block to each modal branch  $\mathcal{F}^l, \mathcal{F}^r$ , and  $\mathcal{F}^f$  independently,

$$\mathcal{F}_{\mathcal{D}}^m = \kappa(\mathcal{F}_{\mathcal{D}-1}^m), \quad (6)$$

where  $\mathcal{D} \in [1, 3]$  denotes layer, and  $m \in \{l, r, f\}$  indicates different modality.  $\kappa$  represents a convolutional layer with batch normalization and ReLU activation.

However, while {IM}<sup>2</sup> addresses some deficiencies in feature representation, this naive approach inevitably introduces redundant features. Inspired by (Song, Zhao, and Skinner 2024b) to adaptively filter each modal feature, we design an MSGF for adaptive gated fusion on each LiDAR and 4D radar scale feature map.

As depicted in Fig. 6, the gated network  $\mathcal{G}$  in MSGF processes input feature maps from LiDAR  $\mathcal{F}^l$ , 4D radar  $\mathcal{F}^r$  and fused counterpart  $\mathcal{F}^f$ . Subsequently, on the LiDAR and 4D radar branches, the adaptive gating weights  $\mathcal{W}^l$  for  $\mathcal{F}^l$  and  $\mathcal{W}^r$  for  $\mathcal{F}^r$  were obtained by a convolution block and sigmoid activation function, respectively. These weights are applied to the initial feature via element-wise multiplication, thus enabling filter  $\mathcal{F}^l$  and  $\mathcal{F}^r$  in the gated mechanism. Formally, the gated network  $\mathcal{G}$  guides  $\mathcal{F}^l$  and  $\mathcal{F}^r$  at convolution layer index  $\mathcal{D}$  to filter out redundant information as following:

$$\begin{aligned} \mathcal{F}_{\mathcal{D}}^m &= \mathcal{G}_{\mathcal{D}}(\mathcal{F}_{\mathcal{D}}^m, \mathcal{F}_{\mathcal{D}}^f), m \in \{l, r\}, \\ \text{and } \mathcal{G}_{\mathcal{D}}^m(\mathcal{F}_{\mathcal{D}}^m, \mathcal{F}_{\mathcal{D}}^f) &= \mathcal{F}_{\mathcal{D}}^m * \delta(\kappa(\mathcal{F}_{\mathcal{D}}^f)), \end{aligned} \quad (7)$$

where  $\kappa$  is a 3x3 convolution block and  $\delta$  a sigmoid function.  $\mathcal{F}^f$  is the fused feature with information about the interactions between modalities. It discerns whether features in  $\mathcal{F}^l$  and  $\mathcal{F}^r$  are helpful or redundant. Using  $\mathcal{F}^f$  for gated filtering can flexibly weight and extract features from  $\mathcal{F}^l$  and  $\mathcal{F}^r$  while significantly reducing feature redundancy.

## Experiments

### Implement Details.

We implement L4DR with PointPillars (Lang et al. 2019), the most commonly used base architecture in radar-based, LiDAR and 4D radar fusion-based 3D object detection. This can effectively verify the effectiveness of our L4DR and avoid unfair comparisons caused by inherent improvements in the base architecture. We set  $\tau$  in section 3.2 as 0.3 while training and 0.2 while inferring (more discussions can be found in supplementary material A.2.). We conduct all experiments with a batch size of 16 on 2 RTX 3090 GPUs. Other parameter settings refer to the default official configuration in the OpenPCDet (Team et al. 2020) tool.

Methods	Modality	Metric	Total	Normal	Overcast	Fog	Rain	Sleet	Lightsnow	Heavysnow
RTNH (NeurIPS 2022)	4DR	$AP_{BEV}$	41.1	41.0	44.6	45.4	32.9	50.6	81.5	56.3
		$AP_{3D}$	37.4	37.6	42.0	41.2	29.2	49.1	63.9	43.1
PointPillars (CVPR 2019)	L	$AP_{BEV}$	49.1	48.2	53.0	45.4	44.2	45.9	74.5	53.8
		$AP_{3D}$	22.4	21.8	28.0	28.2	27.2	22.6	23.2	12.9
RTNH (NeurIPS 2022)	L	$AP_{BEV}$	66.3	65.4	87.4	83.8	73.7	48.8	78.5	48.1
		$AP_{3D}$	37.8	39.8	46.3	59.8	28.2	31.4	50.7	24.6
InterFusion (IROS 2023)	L+4DR	$AP_{BEV}$	52.9	50.0	59.0	80.3	50.0	22.7	72.2	53.3
		$AP_{3D}$	17.5	15.3	20.5	47.6	12.9	9.33	56.8	25.7
3D-LRF (CVPR 2024)	L+4DR	$AP_{BEV}$	<u>73.6</u>	<u>72.3</u>	<u>88.4</u>	<u>86.6</u>	<u>76.6</u>	47.5	<u>79.6</u>	<b>64.1</b>
		$AP_{3D}$	<u>45.2</u>	<u>45.3</u>	<u>55.8</u>	51.8	<u>38.3</u>	23.4	<b>60.2</b>	<u>36.9</u>
L4DR (Ours)	L+4DR	$AP_{BEV}$	<b>77.5</b>	<b>76.8</b>	<b>88.6</b>	<b>89.7</b>	<b>78.2</b>	<b>59.3</b>	<b>80.9</b>	<u>53.8</u>
		$AP_{3D}$	<b>53.5</b>	<b>53.0</b>	<b>64.1</b>	<b>73.2</b>	<b>53.8</b>	<b>46.2</b>	52.4	<b>37.0</b>

Table 2: Quantitative results of different 3D object detection methods on K-Radar dataset. We present the modality of each method (L: LiDAR, 4DR: 4D radar) and detailed performance for each weather condition. Best in **bold**, second in underline.

### Dataset and Evaluation Metrics

**K-Radar dataset.** The K-Radar dataset (Paek, Kong, and Wijaya 2022) contains 58 sequences with 34944 frames of 64-line LiDAR, camera, and 4D radar data in various weather conditions. According to the official K-Radar split, we used 17458 frames for training and 17536 frames for testing. We adopt two evaluation metrics for 3D object detection:  $AP_{3D}$  and  $AP_{BEV}$  of the class "Sedan" at IoU = 0.5. We also provide more quantitative results for other IoU thresholds as well as using the latest v2.1 version of the label (see supplementary material).

**View-of-Delft (VoD) dataset.** The VoD dataset (Palffy et al. 2022) contains 8693 frames of 64-line LiDAR, camera, and 4D radar data. Following the official partition, we divided the dataset into a training and validation set with 5139 and 1296 frames. Meanwhile, to explore the performance under different fog intensities, following a series of previous work (Qian et al. 2021; Li et al. 2022), we similarly performed fog simulations (Hahner et al. 2021) (with fog level  $\mathcal{L}$  from 0 to 4, fog density ( $\alpha$ ) = [0.00, 0.03, 0.06, 0.10, 0.20]) on the VoD dataset and 4D Radar remains unchanged to simulate weather robustness. We express this as the **Vod-Fog** dataset in the following. Noteworthy, we used two evaluation metrics groups. The VoD official metrics are used to compare better the results reported by previous state-of-the-art methods. The KITTI official metrics are for better demonstrating and analyzing the performance of "easy", "moderate" and "hard" objects with different difficulties under foggy weather, for more details of the metrics see the supplementary material.

### Results on K-Radar Adverse Weather Dataset

Following 3D-LRF (Chae, Kim, and Yoon 2024), we compare our L4DR with LiDAR only, 4D radar only, and LiDAR-4D radar fusion-based 3D object detection methods: PointPillars (Lang et al. 2019), RTNH (Paek, KONG, and Wijaya 2022), InterFusion (Wang et al. 2022b) and 3D-LRF (Chae, Kim, and Yoon 2024). The results in Table 2 highlight the

superior performance of our L4DR model in all weather conditions. Our L4DR model surpasses 3D-LRF by 8.3% in total  $AP_{3D}$ . This demonstrates that compared to previous fusion frameworks, our proposed fusion method utilizes the advantages of LiDAR and 4D Radar more effectively. Note that we only compare 3D-LRF (Chae, Kim, and Yoon 2024) on the K-Radar dataset because its code is not open-sourced, the results of 3D-LRF are available on the K-Radar dataset only.

Meanwhile, it is worth noting that the performance in many bad weather conditions instead significantly exceeds the performance in normal weather (e.g., Overcast, Fog, etc.). This is a phenomenon also reflected in the official benchmark of the K-Radar dataset, and we discuss this counter-intuitive phenomenon in detail in the supplementary material. We also discuss other valuable results such as different IoU thresholds and new version labels.

### Results on Vod-Fog Simulated Dataset

We evaluated our L4DR model in comparison with LiDAR and 4D radar fusion methods using the Vod-Fog dataset using the KITTI metrics across varying levels of fog. Table 3 demonstrates that our L4DR model outperforms LiDAR-only PointPillars in different difficulty categories and fog intensities. Particularly in the most severe fog conditions (fog level = 4), our L4DR model achieves performance improvements of 17.43%, 17.8%, and 24.81% mAP in moderate difficulty categories, surpassing the gains obtained by InterFusion. Furthermore, our approach consistently exhibits superior performance compared to InterFusion across various scenarios, showcasing the adaptability of our L4DR fusion under adverse weather conditions.

### Results on VoD Dataset

We compared our L4DR fusion performance with different state-of-the-art methods of different modalities on the VoD dataset with *VoD metric*. As shown in Table 4, our L4DR fusion outperforms the existing LiDAR and 4D radar fusion method InterFusion (Wang et al. 2022b) in all categories. We

Fog Level	Methods	Modality	Car (IoU = 0.5)			Pedestrian (IoU = 0.25)			Cyclist (IoU = 0.25)		
			Easy	Mod.	Hard	Easy	Mod.	Hard	Easy	Mod.	Hard
0 (W/o Fog)	PointPillars	L	84.9	73.5	67.5	62.7	58.4	53.4	85.5	79.0	72.7
	InterFusion	L+4DR	67.6	65.8	58.8	73.7	70.1	64.7	90.3	87.0	81.2
	L4DR (Ours)	L+4DR	<b>85.0</b>	<b>76.6</b>	<b>69.4</b>	<b>74.4</b>	<b>72.3</b>	<b>65.7</b>	<b>93.4</b>	<b>90.4</b>	<b>83.0</b>
1	PointPillars	L	79.9	72.7	67.0	59.9	55.6	50.5	85.5	78.2	72.0
	InterFusion	L+4DR	66.1	64.0	56.9	74.0	70.6	64.5	91.6	87.4	82.0
	L4DR (Ours)	L+4DR	<b>77.9</b>	<b>73.2</b>	<b>67.8</b>	<b>75.4</b>	<b>72.1</b>	<b>66.7</b>	<b>93.8</b>	<b>91.0</b>	<b>83.2</b>
2	PointPillars	L	67.0	51.4	44.4	53.1	47.2	42.7	69.6	62.7	57.2
	InterFusion	L+4DR	56.0	48.5	41.5	<b>63.2</b>	57.8	52.9	77.3	71.1	66.2
	L4DR (Ours)	L+4DR	<b>68.5</b>	<b>56.4</b>	<b>49.3</b>	63.1	<b>59.9</b>	<b>55.1</b>	<b>82.7</b>	<b>70.8</b>	<b>70.7</b>
3	PointPillars	L	44.5	31.9	27.0	40.2	37.7	34.0	53.2	46.7	41.8
	InterFusion	L+4DR	41.2	33.1	27.0	52.9	49.2	44.8	59.9	57.7	53.1
	L4DR (Ours)	L+4DR	<b>46.2</b>	<b>41.4</b>	<b>34.6</b>	<b>53.5</b>	<b>50.6</b>	<b>46.2</b>	<b>72.2</b>	<b>67.7</b>	<b>60.9</b>
4	PointPillars	L	13.0	8.77	7.19	10.6	12.9	11.3	6.15	4.89	4.57
	InterFusion	L+4DR	15.2	10.8	8.40	25.7	25.1	22.6	6.68	7.95	6.99
	L4DR (Ours)	L+4DR	<b>26.9</b>	<b>26.2</b>	<b>21.6</b>	<b>33.1</b>	<b>30.7</b>	<b>27.9</b>	<b>30.3</b>	<b>29.7</b>	<b>26.3</b>

Table 3: Quantitative results of different methods on Vod-Fog dataset with the KITTI metric under various fog levels.

outperformed by 6.8% in the Cyc. class in the Driving Area. Meanwhile, our L4DR also significantly outperforms other modality-based state-of-the-art methods such as LXL (Xiong et al. 2024). These experimental results demonstrate that our method can comprehensively fuse the two modalities of LiDAR and 4D radar. As a consequence, our L4DR method also shows superior performance even in clear weather.

Methods	Modality	Entire Area			Driving Area		
		Car	Ped.	Cyc.	Car	Ped.	Cyc.
Pointpillars	4DR	39.7	31.0	65.1	71.6	40.5	87.8
LXL	4DR	32.8	39.7	68.1	70.3	47.3	87.9
FUTR3D	C+4DR	46.0	35.1	66.0	78.7	43.1	86.2
BEVFusion	C+4DR	37.9	41.0	69.0	70.2	45.9	89.5
RCFusion	C+4DR	41.7	39.0	68.3	71.9	47.5	88.3
LXL	C+4DR	42.3	49.5	77.1	72.2	58.3	88.3
Pointpillars	L	66.0	55.6	75.0	88.7	68.4	88.4
InterFusion	L+4DR	66.5	64.5	78.5	90.7	72.0	88.7
L4DR (Ours)	L+4DR	<b>69.1</b>	<b>66.2</b>	<b>82.8</b>	<b>90.8</b>	<b>76.1</b>	<b>95.5</b>

Table 4: Comparing L4DR with different state-of-the-art methods of different modalities on VoD dataset with the VoD metrics. The best performances are highlighted in **bold**.

## Ablation study

**Effect of each component.** We systematically evaluated each component, with the results summarized in Table 5. The 1<sup>st</sup> row represents the performance of the LiDAR-only baseline model. Subsequent enhancements were observed with the addition of MME, as depicted in the 2<sup>nd</sup> row, showcasing significant performance gains attributed to the radar. This performance improvement becomes more significant with increasing fog levels, highlighting the weather resilience of the 4D radar. The 3<sup>rd</sup> row demonstrates further optimization of data fusion between the modalities through noise filtering in the 4D radar using FAD. However, the 4<sup>th</sup> row indicates that the performance boost from incorporating the  $\{\text{IM}\}^2$  model alone was not substantial, primarily due to feature

redundancy introduced by the  $\{\text{IM}\}^2$  backbone. This issue was effectively addressed by utilizing the MSGF module in the 5<sup>th</sup> row, leading to the most optimal performance.

Module				3D mAP				
MME	$\{\text{IM}\}^2$	FAD	MSGF	W/o Fog	$\mathcal{L} = 1$	$\mathcal{L} = 2$	$\mathcal{L} = 3$	$\mathcal{L} = 4$
				70.3	68.9	53.8	38.8	8.92
✓				77.1	75.4	63.2	52.3	23.4
✓	✓			78.7	77.6	63.3	52.2	24.7
✓	✓	✓		78.1	76.8	62.0	52.3	26.5
✓	✓	✓	✓	<b>79.8</b>	<b>78.8</b>	<b>64.7</b>	<b>53.3</b>	<b>28.9</b>

Table 5: Effect of each component proposed in L4DR, tested on Vod-Fog split. 3D mAP represents the average 3D AP of all classes in Mod. difficulty.  $\mathcal{L}$  denotes fog level. The first line does not use any modules indicating PointPillar model that only uses LiDAR.

**Comparison with other multi-modal feature fusion.** We compared different multi-modal feature fusion blocks, including basic concatenation (Concat.) and various attention-based methods such as Transformer-based (Vaswani et al. 2017) Cross-Modal Attention (Cross-Attn.) and Self-Attention (Self-Attn.), SE Block (Hu, Shen, and Sun 2018), and CBAM Block (Woo et al. 2018), see supplementary material for detailed implement. Experimental results (Table 6) show that while attention mechanisms outperform concatenation to some extent, they do not effectively address the challenge of fluctuating features under varying weather conditions. In contrast, our proposed MSGF method, focusing on significant features of LiDAR and 4D radar, achieves superior performance and robustness under different weather.

## Conclusion

In this paper, we analyzed the challenges of fusing LiDAR and 4D radar in adverse weather and proposed L4DR, an effective LiDAR and 4D radar fusion method. We provide an

Fusion	3D mAP				
	W/o Fog	$\mathcal{L} = 1$	$\mathcal{L} = 2$	$\mathcal{L} = 3$	$\mathcal{L} = 4$
Concat.	77.9	76.3	61.9	49.3	17.7
Cross-Attn.	77.2	76.0	63.0	52.7	<b>30.1</b>
Self-Attn.	78.4	77.4	64.3	52.8	25.8
SE Block	77.3	77.9	63.8	50.1	25.0
CBAM Block	78.0	78.1	64.0	52.3	26.4
MSGF (Ours)	<b>79.8</b>	<b>78.8</b>	<b>64.7</b>	<b>53.2</b>	28.8

Table 6: Comparison of multi-modal feature fusion methods on Vod-Fog val split. 3D mAP represents the average 3D AP of all classes in Mod. difficulty.  $\mathcal{L}$  denotes fog level.

innovative and feasible solution for achieving weather-robust outdoor 3D object detection in various weather conditions. Our experiments on VoD and K-Radar datasets have demonstrated the effectiveness and superiority of our method in various simulated fog levels and real-world adverse weather compared to other fusion methods, as well as other modalities. In summary, our proposed L4DR fusion method not only offers a promising solution for robust outdoor 3D object detection in adverse weather conditions but also sets a new benchmark for performance and robustness compared to existing fusion techniques, paving the way for enhanced safety and reliability in autonomous driving and other applications.

**Limitations.** While the introduction of the  $\{\text{IM}\}^2$  and MSGF modules has allowed the model to focus on more salient features, it inevitably introduces additional computations that reduces the computational efficiency to a certain extent. The inference speed is reduced to about **10 FPS**, which is just enough to satisfy the real-time threshold (equal to the LiDAR acquisition frequency), but the computational performance optimization of our L4DR method is a valuable future area of research.

## References

- Balal, N.; Pinhasi, G.; and Pinhasi, Y. 2016. Atmospheric and Fog Effects on Ultra-Wide Band Radar Operating at Extremely High Frequencies. *Sensors*, 16(5): 751.
- Bijelic, M.; Gruber, T.; Mannan, F.; Kraus, F.; Ritter, W.; Dietmayer, K.; and Heide, F. 2020. Seeing Through Fog Without Seeing Fog: Deep Multimodal Sensor Fusion in Unseen Adverse Weather. In *CVPR*.
- Borgefors, G. 1986. Distance transformations in digital images. *Computer vision, graphics, and image processing*, 34(3): 344–371.
- Chae, Y.; Kim, H.; and Yoon, K.-J. 2024. Towards Robust 3D Object Detection with LiDAR and 4D Radar Fusion in Various Weather Conditions. In *Proceedings of the IEEE/CVF Conference on Computer Vision and Pattern Recognition (CVPR)*, 15162–15172.
- Charron, N.; Phillips, S.; and Waslander, S. L. 2018. De-Noising of Lidar Point Clouds Corrupted by Snowfall. In *CRV*.
- Deng, J.; Shi, S.; Li, P.; Zhou, W.; Zhang, Y.; and Li, H. 2021. Voxel R-CNN: Towards High Performance Voxel-based 3D Object Detection. *AAAI*, 35.
- Geiger, A.; Lenz, P.; and Urtasun, R. 2012. Are we ready for autonomous driving? The KITTI vision benchmark suite. In *2012 IEEE Conference on Computer Vision and Pattern Recognition*, 3354–3361.
- Ghita, A.; Antoniusen, B.; Zimmer, W.; Greer, R.; Creß, C.; Møgelmoose, A.; Trivedi, M. M.; and Knoll, A. C. 2024. ActiveAnno3D—An Active Learning Framework for Multi-Modal 3D Object Detection. *arXiv preprint arXiv:2402.03235*.
- Golovachev, Y.; Etinger, A.; Pinhasi, G. A.; and Pinhasi, Y. 2018. Millimeter wave high resolution radar accuracy in fog conditions—theory and experimental verification. *Sensors*, 18(7): 2148.
- Hahner, M.; Sakaridis, C.; Bijelic, M.; Heide, F.; Yu, F.; Dai, D.; and Van Gool, L. 2022. LiDAR Snowfall Simulation for Robust 3D Object Detection. In *CVPR*.
- Hahner, M.; Sakaridis, C.; Dai, D.; and Van Gool, L. 2021. Fog Simulation on Real LiDAR Point Clouds for 3D Object Detection in Adverse Weather. In *ICCV*.
- Han, Z.; Wang, J.; Xu, Z.; Yang, S.; He, L.; Xu, S.; and Wang, J. 2023. 4D Millimeter-Wave Radar in Autonomous Driving: A Survey. *arXiv 2023. arXiv preprint arXiv:2306.04242*.
- Heinzler, R.; Piewak, F.; Schindler, P.; and Stork, W. 2020. CNN-Based Lidar Point Cloud De-Noising in Adverse Weather. *IEEE Robotics and Automation Letters*, 5.
- Hosseinpour, H.; Samadzadegan, F.; and Javan, F. D. 2022. CMGFNet: A deep cross-modal gated fusion network for building extraction from very high-resolution remote sensing images. *ISPRS Journal of Photogrammetry and Remote Sensing*, 184: 96–115.
- Hu, J.; Shen, L.; and Sun, G. 2018. Squeeze-and-excitation networks. In *Proceedings of the IEEE conference on computer vision and pattern recognition*, 7132–7141.
- Huang, X.; Wu, H.; Li, X.; Fan, X.; Wen, C.; and Wang, C. 2024. Sunshine to rainstorm: Cross-weather knowledge distillation for robust 3d object detection. In *Proceedings of the AAAI Conference on Artificial Intelligence*, volume 38, 2409–2416.
- Kilic, V.; Hegde, D.; Sindagi, V. A.; Cooper, A.; Foster, M.; and Patel, V. M. 2021. Lidar Light Scattering Augmentation (LISA): Physics-based Simulation of Adverse Weather Conditions for 3D Object Detection. *ArXiv*.
- Lang, A. H.; Vora, S.; Caesar, H.; Zhou, L.; Yang, J.; and Beijbom, O. 2019. PointPillars: Fast Encoders for Object Detection From Point Clouds. In *2019 IEEE/CVF Conference on Computer Vision and Pattern Recognition (CVPR)*, 12689–12697.
- Li, Y.-J.; O’Toole, M.; and Kitani, K. 2023. St-mvdnet++: Improve vehicle detection with lidar-radar geometrical augmentation via self-training. In *ICASSP 2023-2023 IEEE International Conference on Acoustics, Speech and Signal Processing (ICASSP)*, 1–5. IEEE.
- Li, Y.-J.; Park, J.; O’Toole, M.; and Kitani, K. 2022. Modality-Agnostic Learning for Radar-Lidar Fusion in Vehicle Detection. In *Proceedings of the IEEE/CVF Conference on Computer Vision and Pattern Recognition (CVPR)*, 918–927.



- Paek, D.-H.; Kong, S.-H.; and Wijaya, K. T. 2022. K-radar: 4d radar object detection for autonomous driving in various weather conditions. *Advances in Neural Information Processing Systems*, 35: 3819–3829.
- Paek, D.-H.; KONG, S.-H.; and Wijaya, K. T. 2022. K-Radar: 4D Radar Object Detection for Autonomous Driving in Various Weather Conditions. In Koyejo, S.; Mohamed, S.; Agarwal, A.; Belgrave, D.; Cho, K.; and Oh, A., eds., *Advances in Neural Information Processing Systems*, volume 35, 3819–3829. Curran Associates, Inc.
- Palfy, A.; Pool, E.; Baratam, S.; Kooij, J. F.; and Gavrilu, D. M. 2022. Multi-class road user detection with 3+ 1D radar in the View-of-Delft dataset. *IEEE Robotics and Automation Letters*, 7(2): 4961–4968.
- Qi, C. R.; Yi, L.; Su, H.; and Guibas, L. J. 2017. PointNet++: Deep Hierarchical Feature Learning on Point Sets in a Metric Space. [arXiv:1706.02413](https://arxiv.org/abs/1706.02413).
- Qian, K.; Zhu, S.; Zhang, X.; and Li, L. E. 2021. Robust Multimodal Vehicle Detection in Foggy Weather Using Complementary Lidar and Radar Signals. In *Proceedings of the IEEE/CVF Conference on Computer Vision and Pattern Recognition (CVPR)*, 444–453.
- Shi, S.; Guo, C.; Jiang, L.; Wang, Z.; Shi, J.; Wang, X.; and Li, H. 2020. PV-RCNN: Point-Voxel Feature Set Abstraction for 3D Object Detection. In *CVPR*.
- Shi, S.; Jiang, L.; Deng, J.; Wang, Z.; Guo, C.; Shi, J.; Wang, X.; and Li, H. 2022. PV-RCNN++: Point-Voxel Feature Set Abstraction With Local Vector Representation for 3D Object Detection. *Int. J. Comput. Vision*, 131.
- Song, J.; Zhao, L.; and Skinner, K. A. 2024a. LiRaFusion: Deep Adaptive LiDAR-Radar Fusion for 3D Object Detection. *arXiv preprint arXiv:2402.11735*.
- Song, J.; Zhao, L.; and Skinner, K. A. 2024b. LiRaFusion: Deep Adaptive LiDAR-Radar Fusion for 3D Object Detection. *arXiv preprint arXiv:2402.11735*.
- Sun, S.; and Zhang, Y. D. 2021. 4D automotive radar sensing for autonomous vehicles: A sparsity-oriented approach. *IEEE Journal of Selected Topics in Signal Processing*, 15(4): 879–891.
- Team, O.; et al. 2020. Openpcdet: An open-source toolbox for 3d object detection from point clouds.
- Teufel, S.; Volk, G.; Von Bernuth, A.; and Bringmann, O. 2022. Simulating Realistic Rain, Snow, and Fog Variations For Comprehensive Performance Characterization of LiDAR Perception. In *2022 IEEE 95th Vehicular Technology Conference: (VTC2022-Spring)*.
- Vaswani, A.; Shazeer, N.; Parmar, N.; Uszkoreit, J.; Jones, L.; Gomez, A. N.; Kaiser, Ł.; and Polosukhin, I. 2017. Attention is all you need. *Advances in neural information processing systems*, 30.
- Wang, H.; Shi, C.; Shi, S.; Lei, M.; Wang, S.; He, D.; Schiele, B.; and Wang, L. 2023a. DSVT: Dynamic Sparse Voxel Transformer With Rotated Sets. In *CVPR*.
- Wang, L.; Zhang, X.; Li, J.; Xv, B.; Fu, R.; Chen, H.; Yang, L.; Jin, D.; and Zhao, L. 2022a. Multi-modal and multi-scale fusion 3D object detection of 4D radar and LiDAR for autonomous driving. *IEEE Transactions on Vehicular Technology*.
- Wang, L.; Zhang, X.; Xv, B.; Zhang, J.; Fu, R.; Wang, X.; Zhu, L.; Ren, H.; Lu, P.; Li, J.; and Liu, H. 2022b. InterFusion: Interaction-based 4D Radar and LiDAR Fusion for 3D Object Detection. In *2022 IEEE/RSJ International Conference on Intelligent Robots and Systems (IROS)*, 12247–12253.
- Wang, Y.; Deng, J.; Li, Y.; Hu, J.; Liu, C.; Zhang, Y.; Ji, J.; Ouyang, W.; and Zhang, Y. 2023b. Bi-LRFusion: Bi-Directional LiDAR-Radar Fusion for 3D Dynamic Object Detection. In *Proceedings of the IEEE/CVF Conference on Computer Vision and Pattern Recognition (CVPR)*, 13394–13403.
- Woo, S.; Park, J.; Lee, J.-Y.; and Kweon, I. S. 2018. Cbam: Convolutional block attention module. In *Proceedings of the European conference on computer vision (ECCV)*, 3–19.
- Wu, H.; Wen, C.; Shi, S.; Li, X.; and Wang, C. 2023. Virtual Sparse Convolution for Multimodal 3D Object Detection. In *CVPR*.
- Wu, H.; Zhao, S.; Huang, X.; Wen, C.; Li, X.; and Wang, C. 2024. Commonsense Prototype for Outdoor Unsupervised 3D Object Detection. *arXiv preprint arXiv:2404.16493*.
- Xia, Q.; Deng, J.; Wen, C.; Wu, H.; Shi, S.; Li, X.; and Wang, C. 2023. CoIn: Contrastive Instance Feature Mining for Outdoor 3D Object Detection with Very Limited Annotations. In *Proceedings of the IEEE/CVF International Conference on Computer Vision (ICCV)*, 6254–6263.
- Xiong, W.; Liu, J.; Huang, T.; Han, Q.-L.; Xia, Y.; and Zhu, B. 2024. LXL: LiDAR Excluded Lean 3D Object Detection With 4D Imaging Radar and Camera Fusion. *IEEE Transactions on Intelligent Vehicles*, 9(1): 79–92.
- Xu, G.; Khan, A.; Moshayedi, A. J.; Zhang, X.; and Shuxin, Y. 2022. The Object Detection, Perspective and Obstacles In Robotic: A Review. *EAI Endorsed Transactions on AI and Robotics*, 1: 7–15.
- Xu, Q.; Zhou, Y.; Wang, W.; Qi, C. R.; and Anguelov, D. 2021. SPG: Unsupervised Domain Adaptation for 3D Object Detection via Semantic Point Generation. In *ICCV*.
- Yan, J.; Liu, Y.; Sun, J.; Jia, F.; Li, S.; Wang, T.; and Zhang, X. 2023. Cross modal transformer: Towards fast and robust 3d object detection. In *Proceedings of the IEEE/CVF International Conference on Computer Vision*, 18268–18278.
- Yan, Y.; Mao, Y.; and Li, B. 2018. SECOND: Sparsely Embedded Convolutional Detection. *Sensors*, 18.
- Yang, Z.; Sun, Y.; Liu, S.; and Jia, J. 2020. 3DSSD: Point-Based 3D Single Stage Object Detector. In *CVPR*.

## Appendix / Supplemental Material

### Analysis of Point Distribution of LiDAR and 4D Radar under Different Weather Conditions

Although the weather robustness advantage of 4D radar sensors has been mentioned as a priori knowledge in existing work (Han et al. 2023; Sun and Zhang 2021), this aspect remains less studied. Here, we utilize a variety of real-world adverse weather datasets from K-Radar to examine and corroborate this phenomenon. As depicted in Figure 7, we have compiled plots of the point counts averaged across various types of real-world adverse weather conditions for both LiDAR and 4D radar. It is observed that under different categories of adverse weather conditions, the point counts of LiDAR at different distances from the sensor location (a) exhibit a pronounced decreasing trend, reflecting the significant degradation of LiDAR data quality in adverse weather. In contrast, the point counts of 4D radar at different distances from the sensor location (b) do not show a clear correlation with weather conditions. It is important to note that the large differences in data scenes and dynamic object distributions, and the sensitivity of 4D radar to dynamic objects result in greater fluctuations in point count distribution. However, the lack of correlation between point counts and weather conditions still demonstrates to a certain extent the weather robustness advantage of 4D radar.

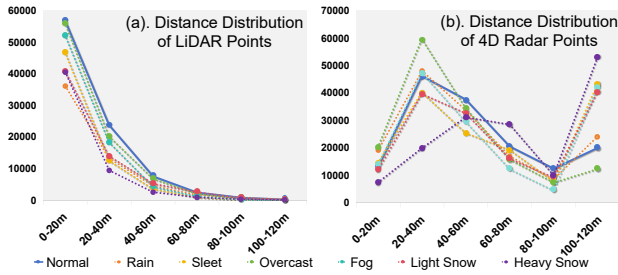


Figure 7: Average number of point distribution of (a) LiDAR and (b) 4D radar with distance under different weather conditions (Normal, Rain, Sleet, Overcast, Fog, Light Snow, and Heavy Snow).

### More Implement Details

For the training strategy, we train the entire network with the loss of 30 epochs. We use Adam optimizer with  $\text{lr} = 1\text{e-}3$ ,  $\beta_1 = 0.9$ ,  $\beta_2 = 0.999$ .

For the K-Radar dataset, we preprocess the 4D radar sparse tensor by selecting only the top 10240 points with high power measurement. We present the set the point cloud range as [0m, 72m] for the X axis, [6.4m, 6.4m] for the Y axis, and [-2m, 6m] for the Z axis setting the same environment with version 1.0 K-Radar. And [0m, 72m] for the X axis, [-16m, 16m] for the Y axis, and [-2m, 7.6m] for the Z axis setting the same environment with version 2.1 K-Radar. The voxel size is set to (0.4m, 0.4m, 0.4m).

For the VoD dataset, following KITTI (Geiger, Lenz, and Urtasun 2012), we calculate the 3D Average Precision (3D AP) across 40 recall thresholds (R40) for different classes.

Also, following VoD’s (Palffy et al. 2022) evaluation metrics, we calculate class-wise AP and mAP averaged over classes. The calculation encompasses the entire annotated region (camera FoV up to 50 meters) and the “Driving Corridor” region ( $[-4\text{ m} \leq x \leq +4\text{ m}, z \leq 25\text{ m}]$ ). For both KITTI metrics and VoD metrics, for AP calculations, we used an IoU threshold specified in VoD, requiring a 50% overlap for car class and 25% overlap for pedestrian and cyclist classes.

### Experimental Visualization Results

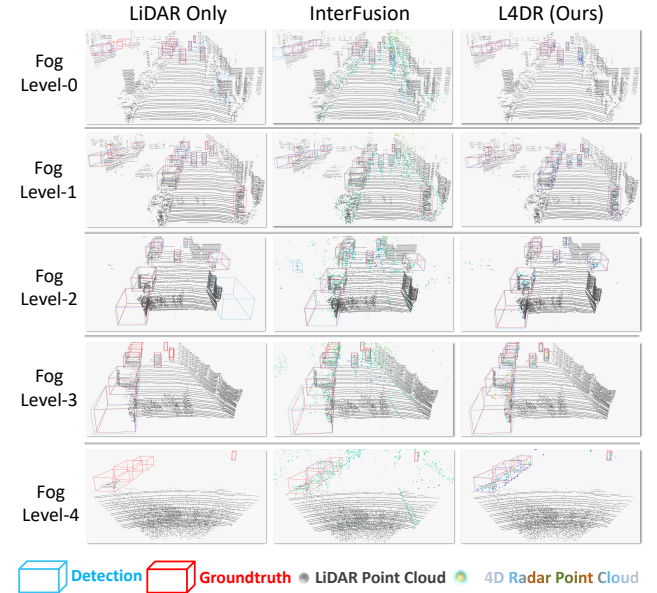


Figure 8: Visualization performance comparison. We visualize object detection results with LiDAR-only (left), InterFusion (middle), and our L4DR (right) on the VoD-fog dataset with different simulated fog levels (0-4, from up to bottom). The red and blue 3D bounding boxes indicate groundtruths and model predictions, respectively, the grey points are LiDAR point clouds and the colored points are 4D radar point clouds. Our L4DR shows the 4D radar point cloud after denoising by the FAD module.

To better visualize how our method improves detection performance, we compare our L4DR with InterFusion (Wang et al. 2022b) under different simulated fog levels, as shown in Figure 8. Our L4DR effectively filters out a substantial amount of noise in 4D radar points (depicted as colored points). Furthermore, our L4DR achieves an effective fusion of LiDAR and 4D radar to increase the precise recall of hard-to-detect objects and reduce false detections.

### Experiments of the hyperparameter $\lambda$ in FAD

We have conducted sufficient experimental discussion on the hyperparameter  $\lambda$  in FAD both in the training and testing stages. The experimental results are shown in Table 7, which shows that too small  $\lambda$  will lead to too much noise residue and an insignificant denoising effect, while too large  $\lambda$  will lose

$\lambda$ in training	$\lambda$ in testing	3D mAP (fog level = 0)	3D mAP (fog level = 1)	3D mAP (fog level = 2)	3D mAP (fog level = 3)	3D mAP (fog level = 4)
0.1	0.1	77.56	77.03	62.40	50.11	25.27
	0.2	75.92	75.79	61.09	49.00	25.28
	0.3	75.46	74.46	60.84	48.84	25.72
	0.5	73.57	71.79	59.10	47.15	24.99
0.2	0.1	77.59	77.43	64.06	52.57	23.90
	0.2	77.21	76.63	62.94	51.10	23.99
	0.3	75.84	75.23	62.15	50.44	23.97
	0.5	73.73	72.61	59.41	48.87	22.40
0.3	0.1	79.51	78.77	63.78	52.95	25.94
	0.2	<b>79.80</b>	<b>78.84</b>	<b>64.73</b>	53.26	<b>28.87</b>
	0.3	79.67	77.91	63.33	52.02	26.28
	0.5	76.71	75.75	61.28	51.56	26.46
0.5	0.1	77.18	76.67	62.35	51.45	24.30
	0.2	78.91	77.87	63.61	<b>53.49</b>	28.49
	0.3	79.47	78.35	63.57	52.22	27.19
	0.5	78.57	77.12	62.47	51.18	26.29

Table 7: Performance with different hyperparameters  $\lambda$  in FAD both in the training and testing stages.

a large number of foreground points affecting the detection of the object. Moreover, the performance degree of different  $\lambda$  under different fog levels is also different, which is due to the different importance of 4D radar under different fog levels. In the end, we chose the setting with the best overall performance with  $\lambda = 0.3$  for training and  $\lambda = 0.2$  for testing, which is also in line with our expectations. Firstly,  $\lambda$  cannot be used with the 0.5 threshold for conventional binary classification, which needs to be appropriately lowered. Secondly, the threshold  $\lambda$  for training should be slightly higher than that for testing due to the increased number of foreground points caused by the data augmentations, such as Ground Truth Sampling.

### Foreground Semantic Segmentation Results in FAD

$\lambda$ in testing	Recall	IoU	PA
0.1	84.35	38.07	88.43
0.2	78.04	50.11	93.45
0.3	73.15	54.14	94.78
0.5	65.52	54.39	95.52

Table 8: Experimental Recall, IoU, and PA performance results of foreground semantic segmentation in FAD ( $\lambda$  in training is 0.3).

We also tested the experimental results of FAD for the denoising stage in semantic segmentation. We used Recall, IoU, and Point Accuracy (PA) as the evaluation metrics, as shown in Table 8. With the increase of hyperparameter  $\lambda$ , Recall decreases and IoU and PA gradually increase. At  $\lambda =$

0.5, we obtain the best IoU and PA, but the lowest recall. It verifies the correctness of our denoising algorithm for semantic segmentation. However, we find that the performance of the 3D object detection task is not as good when  $\lambda$  is higher because losing more foreground points is more detrimental to object detection than retaining some background points.

### More Performance on K-Radar Dataset

The main text is bound by space constraints and only results using IoU=0.5 and v1.0 labeling are shown on K-Radar. Here we additionally show results using IoU=0.3 with v1.0 labels as in Table. 9 and results using IoU=0.3 with v2.0 labels as in Table. 10. The experimental results all demonstrate the superior performance of our L4DR.

### More Fusion Details

Below we present the implementation details of the individual fusion methods compared in Table 6 of the main text, all of which are implemented on the PointPiillars baseline.

**Concat.** We directly concatenate the pseudo-images of LiDAR with 4DRadar in the channel dimension after PointPillar coding.

**Cross-Attn.** We used a 32-dimensional sin/cos position-encoded 4-head attention layer to calculate the Cross-Modal Pillar feature added to the 4DRadar Pillar feature from the LiDAR Pillar feature to the 4DRadar P illar feature, and also to calculate the 4DRadar Pillar feature to the LiDAR P illar feature's Cross-Modal Pillar feature and added to the LiDAR Pillar feature.

Methods	Modality	IoU	Metric	Total	Normal	Overcast	Fog	Rain	Sleet	Lightsnow	Heavysnow
RTNH (NeurIPS 2022)	4DR	0.5	$AP_{BEV}$	41.1	41.0	44.6	45.4	32.9	50.6	81.5	56.3
			$AP_{3D}$	37.4	37.6	42.0	41.2	29.2	49.1	63.9	43.1
		0.3	$AP_{BEV}$	36.0	35.8	41.9	44.8	30.2	34.5	63.9	55.1
			$AP_{3D}$	14.1	19.7	20.5	15.9	13.0	13.5	21.0	6.36
PointPillars (CVPR 2019)	L	0.5	$AP_{BEV}$	49.1	48.2	53.0	45.4	44.2	45.9	74.5	53.8
			$AP_{3D}$	22.4	21.8	28.0	28.2	27.2	22.6	23.2	12.9
		0.3	$AP_{BEV}$	51.9	51.6	53.5	45.4	44.7	54.3	81.2	55.2
			$AP_{3D}$	47.3	46.7	51.9	44.8	42.4	45.5	59.2	55.2
RTNH (NeurIPS 2022)	L	0.5	$AP_{BEV}$	66.3	65.4	87.4	83.8	73.7	<u>48.8</u>	78.5	48.1
			$AP_{3D}$	37.8	39.8	46.3	<u>59.8</u>	28.2	<u>31.4</u>	50.7	24.6
		0.3	$AP_{BEV}$	76.5	76.5	88.2	<u>86.3</u>	77.3	55.3	81.1	59.5
			$AP_{3D}$	72.7	73.1	76.5	84.8	64.5	<u>53.4</u>	80.3	52.9
InterFusion (IROS 2023)	L+4DR	0.5	$AP_{BEV}$	52.9	50.0	59.0	80.3	50.0	22.7	72.2	53.3
			$AP_{3D}$	17.5	15.3	20.5	47.6	12.9	9.33	<u>56.8</u>	25.7
		0.3	$AP_{BEV}$	57.5	57.2	60.8	81.2	52.8	27.5	72.6	57.2
			$AP_{3D}$	53.0	51.1	58.1	80.9	40.4	23.0	71.0	55.2
3D-LRF (CVPR 2024)	L+4DR	0.5	$AP_{BEV}$	<u>73.6</u>	<u>72.3</u>	<u>88.4</u>	<u>86.6</u>	<u>76.6</u>	47.5	<u>79.6</u>	<b>64.1</b>
			$AP_{3D}$	<u>45.2</u>	<u>45.3</u>	<u>55.8</u>	51.8	<u>38.3</u>	23.4	<b>60.2</b>	<u>36.9</u>
		0.3	$AP_{BEV}$	<b>84.0</b>	<u>83.7</u>	<u>89.2</u>	<b>95.4</b>	<u>78.3</u>	<u>60.7</u>	<u>88.9</u>	<b>74.9</b>
			$AP_{3D}$	74.8	<b>81.2</b>	<b>87.2</b>	<u>86.1</u>	<u>73.8</u>	49.5	<b>87.9</b>	<b>67.2</b>
L4DR (Ours)	L+4DR	0.5	$AP_{BEV}$	<b>77.5</b>	<b>76.8</b>	<b>88.6</b>	<b>89.7</b>	<b>78.2</b>	<b>59.3</b>	<b>80.9</b>	<u>53.8</u>
			$AP_{3D}$	<b>53.5</b>	<b>53.0</b>	<b>64.1</b>	<b>73.2</b>	<b>53.8</b>	<b>46.2</b>	52.4	<b>37.0</b>
		0.3	$AP_{BEV}$	<u>79.5</u>	<b>86.0</b>	<b>89.6</b>	<u>89.9</u>	<b>81.1</b>	<b>62.3</b>	<b>89.1</b>	<u>61.3</u>
			$AP_{3D}$	<b>78.0</b>	<u>77.7</u>	<u>80.0</u>	<b>88.6</b>	<b>79.2</b>	<b>60.1</b>	<u>78.9</u>	<u>51.9</u>

Table 9: Quantitative results of different 3D object detection methods on K-Radar dataset. We present the modality of each method (L: LiDAR, 4DR: 4D radar) and detailed performance for each weather condition. Best in **bold**, second in underline.

Class	Method	Modality	Total	Normal	Li. Snow	He. Snow	Rain	Sleet	Overcast	Fog
Sedan	Pointpillars* (CVPR2019)	4DR	42.8	35.0	53.6	48.3	37.4	37.5	53.9	77.3
	RTNH(NIPS2022)	4DR	48.2	35.5	65.6	52.6	40.3	48.1	58.8	79.3
	Pointpillars* (CVPR2019)	L	69.7	68.1	79.0	51.5	77.7	59.1	79.0	89.2
	InterFusion* (IROS2022)	L+4DR	69.9	69.0	79.1	51.7	77.1	58.9	77.9	<b>89.5</b>
	L4DR (Ours)	L+4DR	<b>75.8</b>	<b>74.6</b>	<b>87.5</b>	<b>58.4</b>	<b>77.8</b>	<b>61.4</b>	<b>79.2</b>	89.3
Bus or Truck	Pointpillars* (CVPR2019)	4DR	29.4	25.8	64.1	34.9	0.0	18.0	21.5	-
	RTNH(NIPS2022)	4DR	34.4	25.3	78.2	46.3	0.0	28.5	31.1	-
	Pointpillars* (CVPR2019)	L	53.8	52.9	84.1	50.7	3.7	61.8	77.3	-
	InterFusion* (IROS2022)	L+4DR	56.9	56.2	<b>85.7</b>	40.5	6.4	<b>70.6</b>	80.5	-
	L4DR (Ours)	L+4DR	59.7	59.4	84.4	<b>51.9</b>	<b>8.1</b>	66.1	<b>86.4</b>	-

Table 10: Performance Comparing L4DR under each type of real-world weather condition. The best performances are highlighted in **bold**. \* indicates our reproduction using open-source code from original authors. - indicates that there is no object or the original author does not report performance. L indicates LiDAR and 4DR indicates 4D radar.

**Self-Attn.** We use a 32-dimensional sin/cos position-encoded 4-head attentional layer to compute self-attentional features on the last two BEV features of the 2D Backbone and add them to the original features.

**SE Block.** We use 2x Squeeze’s SEBlock to compute SE features for each BEV feature of the 2D Backbone and add them to the original feature.

**CBAM Block.** We use CBAM Block to compute SE features for each BEV feature of the 2D Backbone and add them to the original feature.